Geophysical Journal International

Geophys. J. Int. (2015) **201,** 1722–1737 doi: 10.1093/gji/ggv069
GJI Seismology

Using glacier seismicity for phase velocity measurements and Green's function retrieval

Fabian Walter,[1,2] Philippe Roux,[1,2] Claudia Roeoesli,[3,4,5] Albanne Lecointre,[1,2] Debi Kilb[6] and Pierre-François Roux[7]

[1] *Université Grenoble Alpes, ISTerre, F-38041 Grenoble, France. E-mail: fwalter@vaw.baug.ethz.ch*
[2] *CNRS, ISTerre, F-38041 Grenoble, France*
[3] *Institute of Geophysics, ETH Zürich, Zürich, Switzerland*
[4] *Laboratory of Hydraulics, Hydrology and Glaciology (VAW), ETH Zürich, Zürich, Switzerland*
[5] *Swiss Seismological Service (SED), ETH Zürich, Zürich, Switzerland*
[6] *Scripps Institution of Oceanography, University of California, San Diego, La Jolla, CA, USA*
[7] *Magnitude (a Baker Hughes & CGG company), Houston, TX, USA*

Accepted 2015 February 10. Received 2014 November 18; in original form 2014 July 28

SUMMARY

High-melt areas of glaciers and ice sheets foster a rich spectrum of ambient seismicity. These signals not only shed light on source mechanisms (e.g. englacial fracturing, water flow, iceberg detachment, basal motion) but also carry information about seismic wave propagation within glacier ice. Here, we present two approaches to measure and potentially monitor phase velocities of high-frequency seismic waves ($\geq$1 Hz) using naturally occurring glacier seismicity. These two approaches were developed for data recorded by on-ice seasonal seismic networks on the Greenland Ice Sheet and a Swiss Alpine glacier. The Greenland data set consists of continuous seismograms, dominated by long-term tremor-like signals of englacial water flow, whereas the Alpine data were collected in triggered mode producing 1–2 s long records that include fracture events within the ice ('icequakes'). We use a matched-field processing technique to retrieve frequency-dependent phase velocity measurements for the Greenland data. In principle, this phase dispersion relationship can be inverted for ice sheet thickness and bed properties. For these Greenland data, inversion of the dispersion curve yields a bedrock depth of 541 m, which may be too small by as much as 35 per cent. We suggest that the discrepancy is due to lateral changes in ice sheet depth and bed properties beneath the network, which may cause unaccounted mixing of surface wave modes in the dispersion curve. The Swiss Alpine icequake records, on the other hand, allow for reconstruction of the impulse response between two seismometers. The direct and scattered wave fields from the vast numbers of icequake records (tens of thousands per month) can be used to measure small changes in englacial velocities and thus monitor structural changes within the ice.

Key words: Glaciology; Seismic tomography.

INTRODUCTION

Seismological techniques have become an important component of glaciological research. With the advent of portable digital instrumentation, seismometer installation is now possible even in remote and/or hostile environments such as Polar Regions, glacier ablation zones, and other types of mountainous terrain. As seismometer networks can target seismogenic processes at large distances, they often constitute a valuable supplement to conventional glaciological point measurements.

To date, passive seismic studies have focused primarily on source processes. Monitoring high-frequency (>1 Hz) 'icequake' activity, recent investigations have led to new insights into englacial fracture propagation (Bassis *et al.* 2007; Walter *et al.* 2009; Carmichael *et al.* 2012; Mikesell *et al.* 2012; Pomeroy *et al.* 2013; Heeszel *et al.* 2014) and basal processes (Smith *et al.* 2006; Danesi *et al.* 2007; Walter *et al.* 2008; Dalban Canassy *et al.* 2013; Moore *et al.* 2013; Thelen *et al.* 2013; Winberry *et al.* 2013; Allstadt & Malone 2014). Similarly, the high-frequency signature of iceberg calving has allowed for remote monitoring of ice discharge from tidewater or lake calving glaciers (O'Neel *et al.* 2007; Amundson *et al.* 2008; Richardson *et al.* 2010; Walter *et al.* 2010a; Bartholomaus *et al.* 2012). However, glacier seismicity is not limited to high frequencies. Episodic discharge events from the polar ice sheets (Ekström *et al.* 2003; Tsai & Ekström 2007; Larmat *et al.* 2008; Nettles & Ekström 2010; Chen *et al.* 2011; Veitch & Nettles 2012; Walter *et al.* 2012) and Antarctic ice stream motion (Wiens *et al.* 2008; Walter *et al.* 2011; Zoet *et al.* 2012; Pratt *et al.* 2014)

generate seismic energy at periods as long as tens or even hundreds of seconds.

Recently, investigations have also begun to exploit naturally occurring seismicity to analyse the subsurface structure of ice sheets. For example, Harland *et al.* (2013) used records of basal seismicity to measure elastic anisotropy in Rutford Ice Stream, Antarctica. Zhan *et al.* (2014) focused on ambient seismicity recorded at the surface of the Amery Ice Shelf, Antarctica, to detect seismic resonances within the sub-ice shelf water cavity. Moreover, a number of studies have used subsurface mode conversions of teleseismic waves to determine fabric properties, thicknesses and bed properties of the polar ice sheets (Anandakrishnan & Winberry 2004; Wittlinger & Farra 2012; Chaput *et al.* 2014; Walter *et al.* 2014).

While these results are encouraging, recent developments in crustal seismology provide a rapidly growing toolbox, which has yet to be harnessed in glaciological applications: cross-correlation of ambient seismic noise records allow for imaging and monitoring the Earth's crust at scales ranging from tens of metres to thousands of kilometres. The applied techniques are rooted in the fact that the seismic impulse response between two sites can be reconstructed via cross-correlation of ambient noise seismograms recorded at the two sites (for reviews see Wapenaar *et al.* 2004; Bensen *et al.* 2007; Campillo & Roux 2014). Consequently, passive noise techniques can image and monitor the Earth's crust without the need for artificial seismic sources, such as explosives or hammer blows, which often require expensive and laborious field campaigns.

Here we explore the use of passive seismic techniques for measurements of englacial phase velocities. We develop processing techniques for typical on-ice seismic deployments, consisting of either continuous or triggered records of high-frequency seismicity ($\geq$1 Hz). In future studies, the combination of the two record types could ideally exploit characteristics of ambient seismicity to study subsurface structures of glaciated environments.

We focus on signals of icequakes and water-generated tremor, which often dominate the ambient seismic field in high-melt zones (Walter *et al.* 2008; Röösli *et al.* 2014). Using seismic records from seasonal networks on the Greenland Ice Sheet (GrIS) and Switzerland's Gornergletscher, we derive methods to estimate glacier depths and develop an approach that could monitor a glacier's fracture state. We leverage the fact that glacier ice contains few inhomogeneities (Deichmann *et al.* 2000; Roux *et al.* 2008; Walter *et al.* 2009), which suppresses the development of diffuse waves often used in ambient noise studies of the Earth's crust.

DATA AVAILABILITY AND STUDY SITES

Our investigation uses data from two seasonally installed seismic networks. One was deployed on the GrIS, some 30 km north of the calving front of Jakobshavn Isbræ, the other operated on Gornergletscher, Switzerland's second largest glacier (Figs 1 and 2). With an aperture exceeding 1 km, the GrIS network is more than twice as large as the Gornergletscher network.

The GrIS network was operational from 2011 July 2 to August 17. We use the data from 11 seismometers (models Lennartz LE3D, Lennartz LE3Dlite and Lennartz LE3D/BH) installed either in shallow boreholes (at 2–3 m depth) or directly at the glacier surface. Additional details about the network and other types of glaciological and seismological instrumentation can be found in Röösli *et al.* (2014), Ryser *et al.* (2014) and Andrews *et al.* (2014). The Gornergletscher network recorded between 2006 May 29 and July 28 and

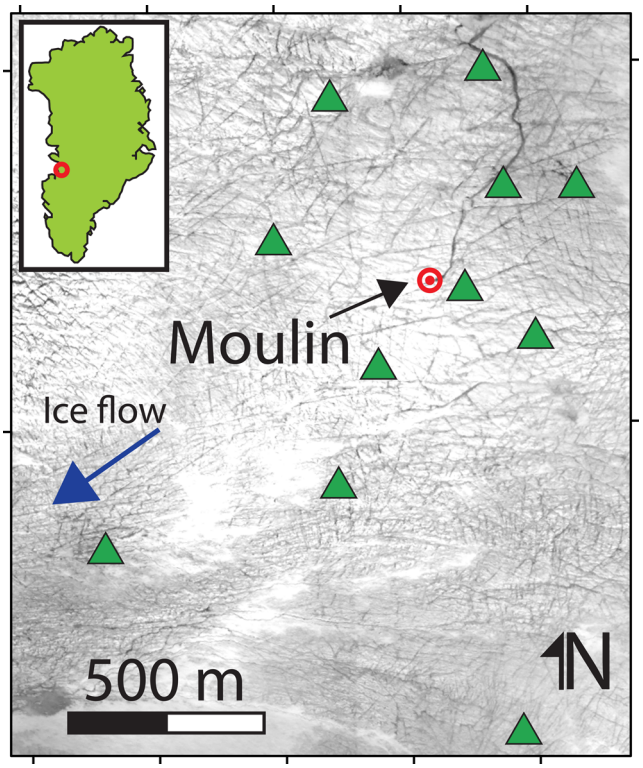

Figure 1. Surface seismometer network (green triangles) and location on the Greenland Ice Sheet shown in the map inset. The background shows a WorldView-2 image (red band, from 2011 June 20, Polar Geospatial Center). Note the presence of surface crevasses and drainage streams, one of which terminated in the moulin (red bulls-eye in Fig. 1) shown in Fig. 3.

consisted of 21 near-surface stations (models Lennartz LE3D and Geospace GS-11D with natural frequencies of 1 and 8 Hz, respectively). Details of this and similar networks on Gornergletscher's tongue can be found in Walter *et al.* (2008) and Walter (2009). The GrIS network operated in continuous mode at a sampling frequency of 500 Hz. In contrast, the Gornergletscher network targeted high-frequency icequakes with impulsive onsets. Recording was therefore performed in triggered mode with 4000 Hz sampling frequency.

The GrIS and Gornergletscher study regions locate in ablation zones and are characterized by high summer surface melt of 2 and 5 m water equivalent, respectively. With an average of 0.27 m d^{-1} (Hoffman *et al.* 2011; McGrath *et al.* 2011), surface flow velocities at the GrIS site are somewhat higher than within the Gornergletscher study region (0.1 m d^{-1}; Huss 2005). Due to the high ablation rates, a network of surface streams forms during the melt season at both sites (Figs 1 and 2). These streams coalesce until they intersect pervasive crevasses constituting hydraulic connections to the glacier bed. As a result, frictional melt during turbulent water flow quickly enlarges crevasses to form efficient englacial drainage channels typically referred to as 'moulins'. A prominent moulin with an intake of 2.5 m^3 s^{-1} (Andrews *et al.* 2014) had formed near the center of the GrIS network (Figs 1 and 3).

GLACIER-RELATED SEISMIC SOURCES

At both study sites, the ice surface exhibits numerous crevasses (Figs 1 and 2) whose formation or extension manifests itself as icequakes (Neave & Savage 1970; Walter *et al.* 2009; Roux *et al.*

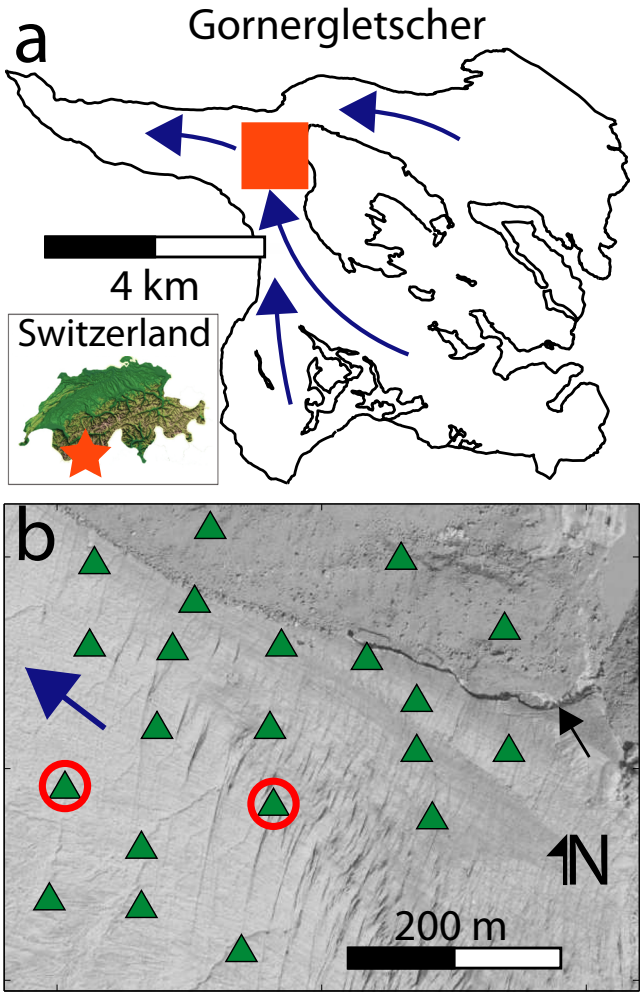

Figure 2. (a) Catchment area of Gornergletscher, location marked in the map inset. Blue arrows indicate approximate flow lines and red square denotes the location of the seismometer network shown in panel (b). (b) Surface seismometer network (green triangles) plotted on top of an ortho photograph. The two circled stations are used for signal cross-correlation. Blue arrow points along glacier flow direction; black arrow highlights a surface drainage channel, which had previously formed during the surface drainage of a seasonal lake.

2010; Mikesell *et al.* 2012). Because of the prevalence of surface crevasses, near-surface seismicity dominates the icequake catalogue although there also exist deep events caused by hydrofracturing and basal motion (Smith *et al.* 2006; Danesi *et al.* 2007; Walter *et al.* 2008; Winberry *et al.* 2013; Dalban Canassy *et al.* 2013; Moore *et al.* 2013; Thelen *et al.* 2013; Allstadt & Malone 2014).

With thousands of recordable icequake events occurring each day, surface icequakes consist mainly of direct waves and cross-correlation of their seismograms recorded at a pair of stations typically give rise to simple, one-sided cross-correlation wavelets (Fig. 4). The icequake signal has a duration of ~0.1–0.2 s with energy concentrated in the 5–30 Hz range (Walter *et al.* 2009). With its maximum amplitude on the vertical component, the Rayleigh wave dominates the seismogram. In contrast, the *P* wave is substantially weaker and for distant events often below the noise level.

The brief duration and weak seismic coda after the Rayleigh wave arrival are the result of limited englacial scattering. This typically allows seismologists to approximate a glacier's seismic velocity model by a homogeneous half-space when locating events or modelling seismic waveforms (e.g. Anandakrishnan & Bentley 1993; Deichmann *et al.* 2000; Walter *et al.* 2009; Carmichael *et al.* 2012; Dalban Canassy *et al.* 2013).

Figure 3. Moulin near the centre of the seismic network shown in Fig. 1. The incised canyon is approximately 2 m wide and at the entrance to the englacial drainage channel several tens of metres deep. Courtesy of Bob Hawley.

Another seismic signal typical for ablation zones is related to water-filled englacial fractures and conduits. These features can generate resonance seismograms, analogous to long-period volcanic tremor (St. Lawrence & Qamar 1979; West *et al.* 2010; Lipovsky & Dunham, 2015). Accordingly, the moulin near the centre of the GrIS network produces a sustained tremor signal, which dominates the ambient ice sheet noise during peak melt hours (Röösli *et al.* 2014). Spectrograms of these tremors exhibit energy primarily between 2 and 8 Hz. Frequency bands of either elevated or suppressed seismic energy can be modulated by moulin water level (Fig. 5) likely reflecting geometry of englacial conduits.

The moulin tremor's signal shown in Fig. 5 is coherent throughout the entire network. This is illustrated in Fig. 6 showing cross-correlations of consecutive five-minute-long seismograms within a two-hour tremor record (Fig. 5). The tremor signal emerges as a nearly constant cross-correlation wavelet with zero lag near 0.1 s. This signal is not disturbed by the frequent occurrence of icequakes, which appear as high-frequency vertical bars in the continuous seismogram (Fig. 6a).

GREENLAND: MATCHED-FIELD PROCESSING OF TREMOR EPISODES

In order to measure phase velocities of moulin tremor signals, we exploit the signal coherence throughout the network. Matched-field

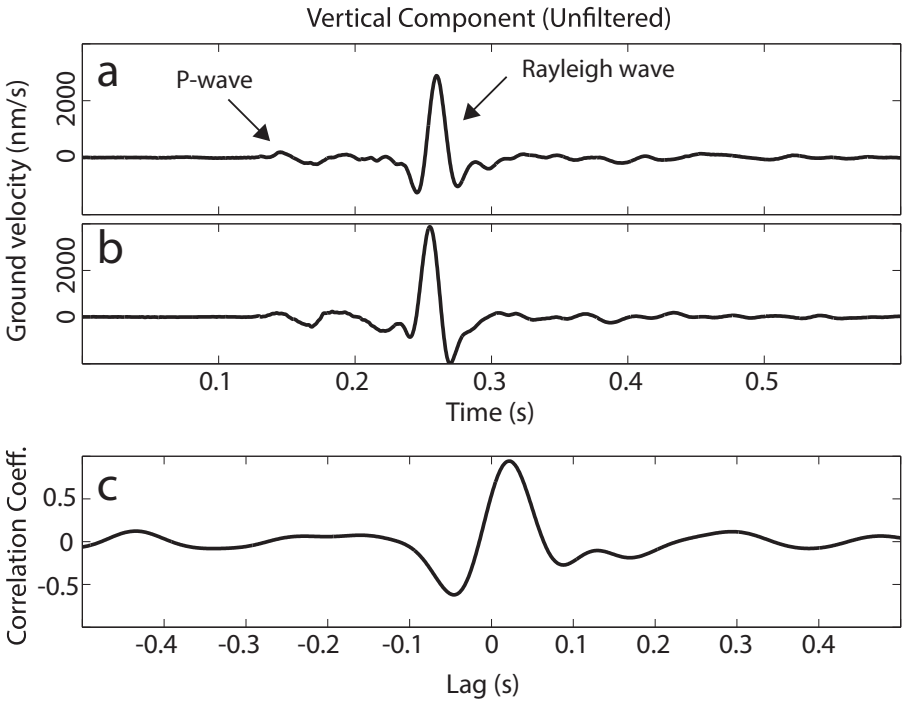

Figure 4. (a and b) Vertical velocity seismograms of surface icequakes recorded at the two stations highlighted in Fig. 2. (c) Cross-correlation of records shown in (a) and (b).

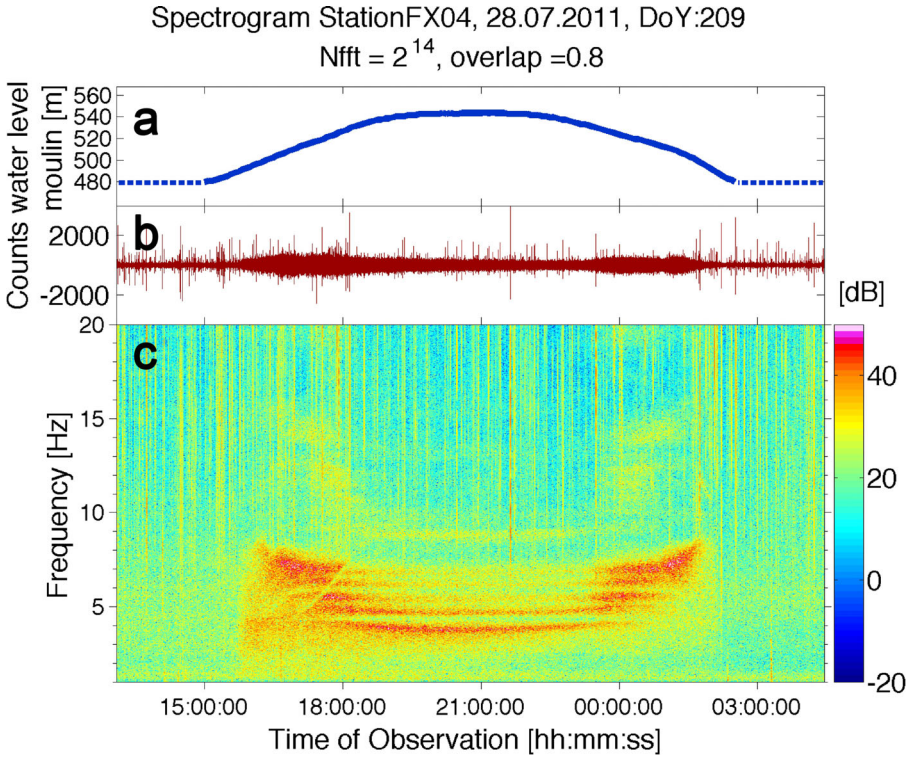

Figure 5. Moulin tremor recorded on 2011 June 28/29. (a) Water level within the moulin. (b) Bandpass-filtered seismogram (2–7 Hz). (c) Water tremor spectrogram showing the excitation of discrete frequency bands. Note the occurrence of high-frequency icequakes shown in panel (b), whose broadband character is visible as vertical bars in the spectrum (panel c).

processing (MFP) is an ideal approach for this endeavour. We briefly outline the key concepts of the MFP technique and refer the reader to Vandemeulebrouck *et al.* (2010), Cros *et al.* (2011), Corciulo *et al.* (2012) and Vandemeulebrouck *et al.* (2013) as well as references therein for further details.

In essence, for each point on a predefined grid (typically spatial coordinates and phase velocity), the MFP algorithm estimates waveform coherence within the monitoring network assuming that the gridpoint is the source of a seismic signal recordable at all stations. Noise sources can thus

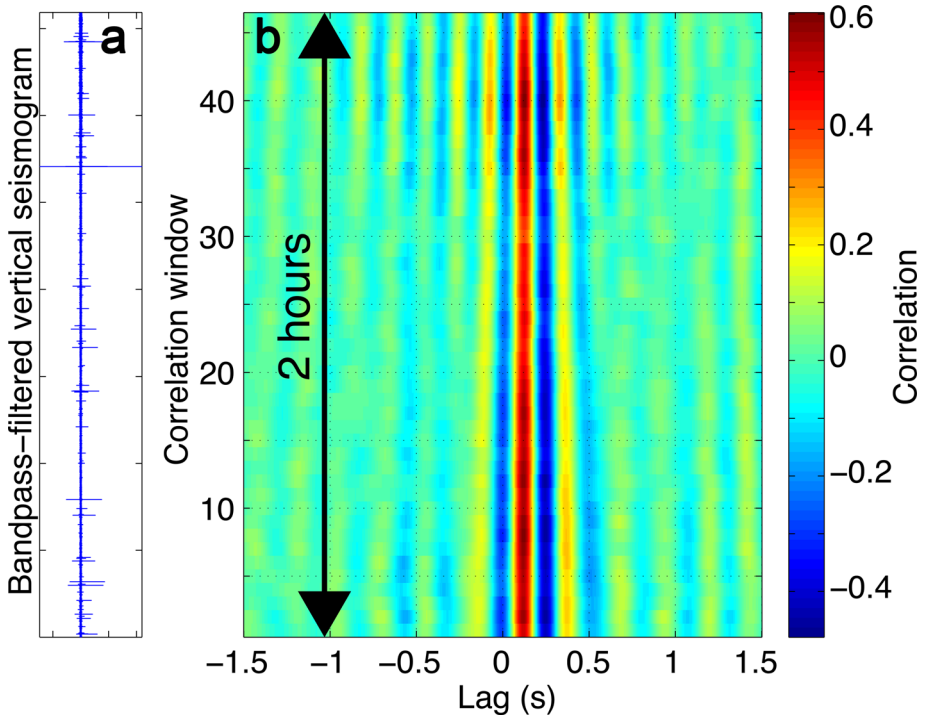

Figure 6. (a) Bandpass-filtered (1–50 Hz) 2-hr seismogram during the tremor episode shown in Fig. 5 (between 22:00:00 and 23:59:00). (b) Time-series of cross-correlation between two stations in the network (using 5-min-long time windows with 50 per cent overlap). Warmer and colder colours correspond to larger positive and negative correlations, respectively. The *y*-axes (time) of both panels are synchronized. Note the relatively constant cross-correlation wavelet representing the persistently emitted tremor signal.

be located by identifying gridpoints with maximum signal coherence.

At a given frequency $\boldsymbol{\omega}$, waveform coherence is measured using a data vector $\mathbf{d}(\boldsymbol{\omega})$ consisting of discrete Fourier transforms of each station record

$$\mathbf{d}(\boldsymbol{\omega}) = [\mathbf{d}(\boldsymbol{\omega})_1, \mathbf{d}(\boldsymbol{\omega})_2, \ldots, \mathbf{d}(\boldsymbol{\omega})_N], \tag{1}$$

where N is the number of stations. The grid search for signal coherence, also known as 'phase matching' or 'beamforming', is accomplished by calculating the inner product between $\mathbf{d}(\boldsymbol{\omega})$ and a replica vector $\mathbf{d}'(\boldsymbol{\omega})$. The latter is the mathematical expression of a theoretical harmonic wave emitted from the gridpoint with a phase depending on the signal frequency and medium velocity. Its amplitude is subject to geometric spreading and other attenuation effects. For seismic surface waves within a lossless homogeneous medium and a seismometer network at the glacier surface, the replica vector is expressed as:

$$\mathbf{d}'_{\mathbf{j}}(\boldsymbol{\omega}, \mathbf{a}_{\mathbf{j}}) = \sqrt{\frac{2}{\pi \mathbf{a}_{\mathbf{j}}}} \mathbf{e}^{-\mathrm{i}\pi/4} \mathbf{e}^{\mathrm{i}\omega a_j/c}, \tag{2}$$

where j is the station index, a_j is the absolute distance between spatial gridpoint and the jth station and c is the medium's phase velocity.

Rather than using the inner product, we can enhance phase matching with the cross-spectral density matrix (CSDM) $\mathbf{K}(\boldsymbol{\omega})$, given by

$$\mathbf{K}(\boldsymbol{\omega}) = \langle \mathbf{d}(\boldsymbol{\omega}) \mathbf{d}^*(\boldsymbol{\omega}) \rangle. \tag{3}$$

Here, '$*$' refers to the complex conjugate and the brackets indicate an ensemble average over a large number of seismic noise windows, for which the outer vector product of $\mathbf{d}(\boldsymbol{\omega})$ and $\mathbf{d}^*(\boldsymbol{\omega})$ is calculated. Phase matching can now be achieved via the conventional processor (Baggeroer *et al.* 1993)

$$\mathbf{B} = \sum_{\omega} \left| \mathbf{d}'^*(\boldsymbol{\omega}, \mathbf{a}) \, \mathbf{K}(\boldsymbol{\omega}) \mathbf{d}'(\boldsymbol{\omega}, \mathbf{a}) \right|. \tag{4}$$

The advantage of the form of eq. (4) is that we can apply singular value decomposition to the CSDM. As dominant noise sources are often associated with large eigenvalues of the CSDM, we can search for weaker noise sources by simply removing the strongest eigenvalue in the singular value decomposition.

LOCATION AND SEPARATION OF TREMOR SOURCES

We apply the MFP to 2-hr-long noise records recorded by the GrIS network. The beamforming is performed at 0.1 Hz increments ranging between 0.2 and 6 Hz. To remove amplitude information from consideration we neglect the factor $\sqrt{\frac{2}{\pi \mathbf{a}_{\mathbf{j}}}} \mathbf{e}^{-\mathrm{i}\pi/4}$ in eq. (2). In this way, we match only the wave phase, which allows us to not favour surface waves over body waves or vice versa. Fig. 7(a) shows the result of the grid search over the two horizontal components and phase velocity (spatial and velocity increments of 20 m and 10 m s^{-1}, respectively). We compute our final results by averaging over all discrete frequencies between 0.2 and 6 Hz. Normalization assures that a beam maximum of 1 represents a perfect phase match throughout the network. Consistent with the Röösli *et al.* (2014) study, the beam maximum indicates the dominant source of ambient seismic noise locates near the central moulin (compare with Fig. 1).

When applying the singular value decomposition to the CSDM we can repeat the phase match for the strongest and second strongest eigenvalues. For the second eigenvalue the central moulin noise

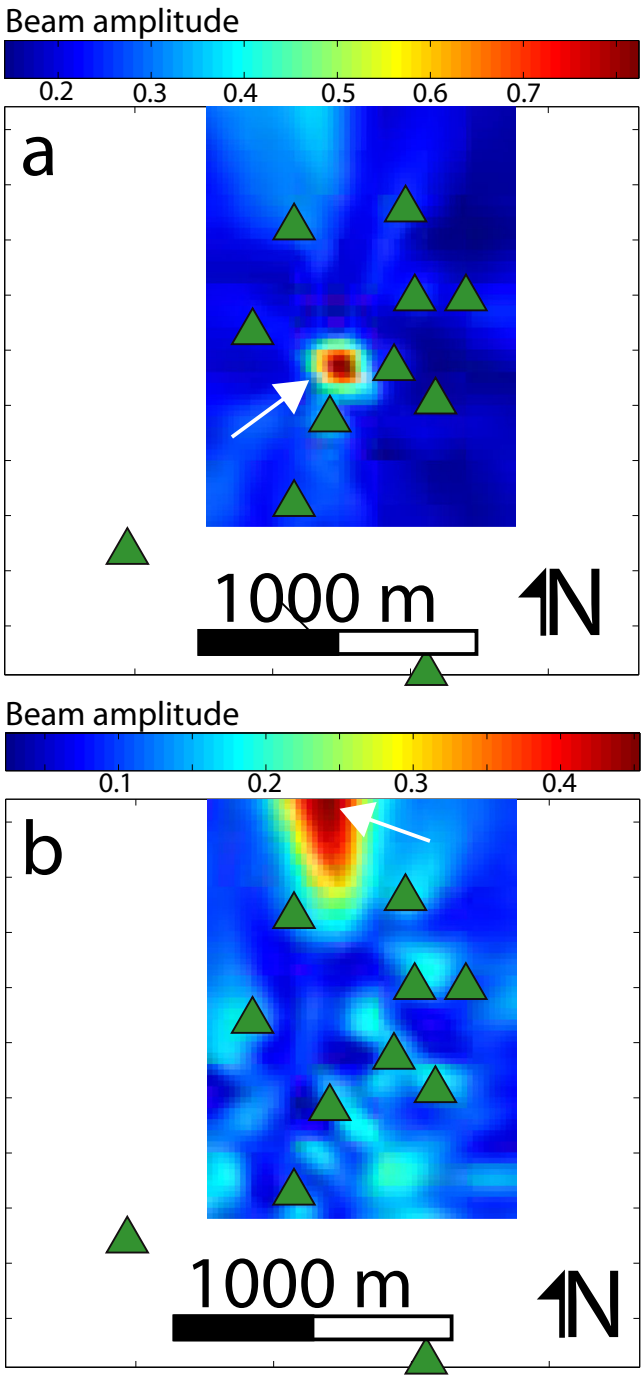

Figure 7. Grid search for matched field processing (MFP) of a 2-hr noise segment recorded on 2011 August 2. The search was performed over Easting, Northing and phase velocity and the results averaged over the 0.2–6 Hz range. (a) A clear maximum in beam amplitude of over 0.82 locates near the moulin, confirming that water flow within this drainage feature is the dominant source of seismic background noise within the network. (b) After singular value decomposition and discarding all but the second strongest eigenvalue, the grid search identifies another source at the Northeast. The moulin noise source within the network, on the other hand, is completely suppressed. Note the different colour bar scales of the two panels. White arrows mark beam maxima in both panels.

source is no longer visible. Instead, a source to the North of the network dominates the phase match (Fig. 7b). The beam maximum is poorly constrained along the axis connecting noise source epicentre and network centre ('radial' direction) and thus may actually locate outside the grid. At this point we assume this maximum corresponds to another moulin, because satellite imagery suggests the presence of several such drainage features in the direction of the beam maximum (L. Andrews, personal communication). However, estimates of drainage basins are needed in order to identify which one of these moulins is emitting the seismic noise, as several candidates locate within 10 km north of the network.

TREMOR SIGNAL DISPERSION MEASUREMENT

Focusing the phase matching on the location of a particular noise source, we can determine the signal's phase velocity as a function of frequency. Our goal is determining the dispersion relationships of Rayleigh waves, which are sensitive to the ice's structure at depths and thus well suitable for imaging purposes. Sources outside the network, such as the northern source associated with the second eigenvalue of the CSDM (Fig. 7b), are more suitable for this task. The central moulin is located within 400 m of most of the stations. For frequencies below 6 Hz and typical *S*-wave velocities in glacier ice of $\sim$1800 m s^{-1} (which are near the Rayleigh wave velocity as explained, for example, in Stein & Wysession 2003), this implies that the stations lie within approximately one wavelength or less of the source. At these close distances near-field effects complicate the interpretation of the dispersion measurements (Aki & Richards 2002). Moreover, the focal depth of the moulin tremor is unknown. Consequently, at close distances we cannot exclude the possibility that seismic body phases interfere with seismic Rayleigh phases. Finally, to detect a source outside the network, the grid search needs to only determine the source azimuth. This eliminates one spatial search parameter and thus minimizes computational expenditure.

The azimuthal grid search is applied to 2-hr-long noise segments. Using the second eigenvalue in the singular value decomposition we search the entire azimuthal range at increments of 10° for normalized beam maxima that exceed 0.5. Subsequently, we focus the beam on this maximum and average the phase velocities within frequency windows of 1 Hz with 80 per cent overlap. We discard measurements with beam averages below 0.5 and repeat the calculation for the next two-hour-long seismic record. The result is a set of Rayleigh wave dispersion measurements providing estimates for mean and standard deviation (Fig. 8). As expected, the phase velocities increase towards longer wavelength (lower frequencies), which are sensitive to the ice sheet bed.

We note that the relatively wide frequency window (1 Hz) was chosen to smooth the resulting dispersion curve. Moreover, moulin tremor signals include frequency bands with little or no energy (Fig. 5). Consequently, narrower frequency windows may be deprived of coherent signals, which would compromise the source separation when applying the singular value decomposition to the CSDM.

ICE SHEET DEPTH ESTIMATIONS

We begin the quantitative interpretation of our processing results with ice sheet depth estimations. To this end, we invert the dispersion curve in Fig. 8 for the underlying velocity model. We employ the enhanced neighbourhood algorithm (Wathelet 2008) to search systematically for a velocity profile, whose Rayleigh wave dispersion

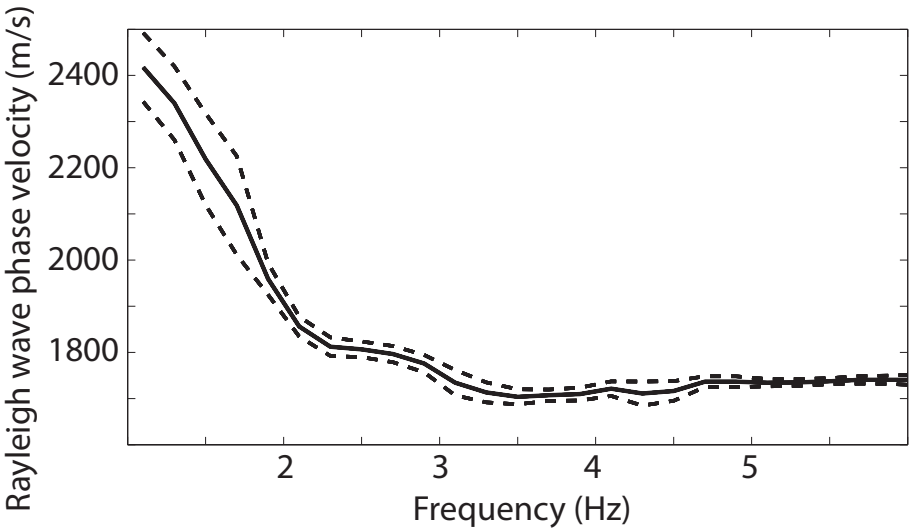

Figure 8. Dispersion relationship obtained from matched field processing using periods when the network was fully operational. Solid and dashed lines mark mean and one standard deviation as calculated from all high-quality dispersion measurements (see text for details) for 2-hr-long noise records. Note that below ~3 Hz, Rayleigh waves become sensitive to the ice sheet bed and their phase velocities therefore increase.

Table 1. Parameter ranges and fixed parameters for grid search to invert the dispersion curve in Fig. 8 for ice sheet thickness. Poisson's ratios of ice and granite were varied between 0.2 and 0.5. Both Poisson's ratio and ice sheet thickness were coupled to the *S*-wave velocity V_S.

Material	Thickness (m)	V_P (m s^{-1})	V_S (m s^{-1})	Density (kg m^{-3})
Ice	200–2000	3870 (fix)	1500–2100	917 (fix)
Granite	∞	200–5000	150–3500	2750 (fix)

matches our measurements. We assume a 1-D, two-layer medium consisting of ice and underlying granite bedrock. This is a simplified approximation and does not include lateral variations in basal topography or allow for the presence of basal till.

The grid search boundaries for seismic velocities, ice thickness, densities and Poisson's ratio are given in Table 1. We fix the seismic *P*-velocity in ice to 3870 m s^{-1} (Kohnen 1974) and couple all varying parameters to the *S*-wave velocity structure. Our results show a 541 m thick ice sheet provides the best fit (Fig. 9). The inversion furthermore determines an *S*-velocity of 1849 and 2619 m s^{-1} in the ice and bedrock layer, respectively. Fig. 9 furthermore shows that the misfit minimum for the ice sheet thickness is well defined. This most likely reflects the fact that the depth-sensitivity of Rayleigh waves reaches a maximum at a depth of approximately 1/3 the wavelength (Li *et al.* 2013). For the inverted *S*-velocity this corresponds to 616 m.

By fixing the *S*-wave velocity for either the ice or bedrock and systematically varying the other, we investigated the sensitivity of the inverted layer thickness. Increases in the ice and bedrock velocities both led to an increase in inverted ice sheet thickness. A 60 m s^{-1} increase in the ice's *S*-velocity resulted in a 45 m increase in ice sheet thickness. On the other hand, the same 60 m s^{-1} increase in the bedrock's *S*-velocity leads to an almost 10 times smaller thickness increase. Moreover, for the ice's *S*-velocity the 60 m s^{-1} increase produces a misfit that is more than doubled, which is in stark contrast to the 3 per cent misfit increase for the same bedrock's *S*-velocity increase. These numerical tests demonstrate that the inverted thickness is particularly sensitive to the *S*-velocity of the ice. However, the determined thickness of 541 m seems robust as variations in the ice's *S*-velocity quickly reduce the fit quality.

Near the central moulin (Fig. 1), hot water drilling measured an ice thickness of up to 620 m (Ryser *et al.* 2014). Furthermore, seismic receiver functions indicate a basal till layer that is at least 80 m thick beneath this region of the network (Walter *et al.* 2014). The seismic velocities of this till layer are poorly constrained, but the residual minima of the receiver function inversion coincide with *S*-wave velocities between 1300 and 1500 m s^{-1} (Fig. 1 in Walter *et al.* 2014). For such seismic velocities the till-bedrock interface constitutes a stronger seismic velocity contrast than the ice-till interface. Accordingly, the top layer inverted with our dispersion inversion includes both the ice and the till layer. This indicates that our inverted bedrock depth of 541 m is at least 159 m too shallow ($620 + 80 - 541$). This 22 per cent discrepancy can be explained with a substantially shallower bedrock depth beneath the southern end of the network as indicated by radar measurements (Steen Savstrup Kristensen, personal communication). This shallow bed region influences the low frequencies of the dispersion curve, in particular. The reason is that in order to capture longer wavelengths (which are sensitive to the glacier bed) the phase measurements require large station separations. The longest inter-station separations, however, require participation of the southern part of the network. Thus, the glacier thickness beneath the southern part of the network may be overrepresented in the dispersion measurement. Perhaps most importantly, the 3-D velocity structure beneath the seismic network can give rise to mode coupling of surface waves (Maupin 2007). If this were the case, our phase velocity measurements would be influenced by several Rayleigh wave modes, which differs from our assumption that the dispersion relationship includes only the fundamental mode.

In addition to the simple ice-over-bedrock model we also conducted a dispersion inversion with an intermediate layer potentially representing subglacial till. This inversion yielded only poorly constrained ice sheet and till layer thicknesses. As seismic velocities within till are highly variable, we have no justification to fix them at a constant value in the inversion merely for the sake of numerical stabilization. To better constrain the dispersion inversion and its

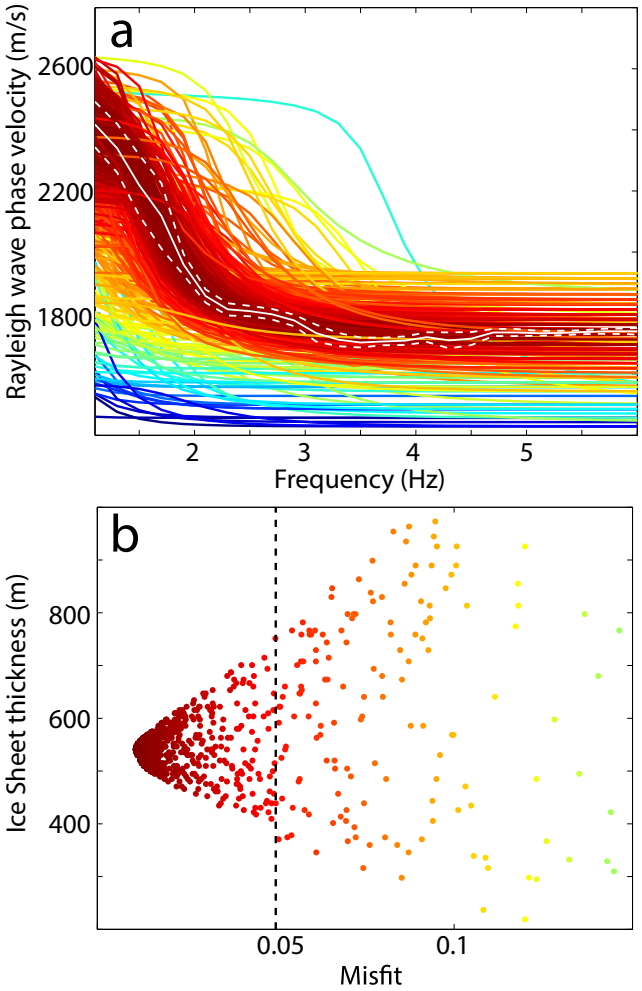

Figure 9. Results of dispersion curve inversion. (a) Colour-coded population (in total 2550) of dispersion curve fits (warmer colours correspond to smaller misfit). The measured dispersion curves (Fig. 8) are overlaid in white. (b) Inverted ice sheet thicknesses versus misfit for each inversion run. For clarity, each dot is colour-coded according to misfit as in panel (a). From visual inspection of panel (a), we obtain a conservative estimate of ice sheet thickness at a misfit of 0.05 (dashed black line).

errors will require accurate bedrock topography maps, dispersion inversions including lateral variations in the velocity model and the use of higher mode Rayleigh waves. As this is beyond the scope of the present study, we conclude that our dispersion-based determination of bedrock depth is subject to an error between 23 and 35 per cent (Fig. 9b).

GORNERGLETSCHER: AUTOMATED ICEQUAKE LOCATIONS

The processing of surface icequake signals on Gornergletscher begins with event epicentre locations. The large number of events detected on Gornergletscher (over 52 000) requires an automated approach. We use the method of Roux *et al.* (2010), which employs cross-correlations to automatically measure differences in Rayleigh wave arrival times. The triggered Gornergletscher data set is well suited for this task, because a relatively small seismic network recorded these data. This increases Rayleigh waveform coherence throughout the network, which is necessary in obtaining a sufficient amount of differential arrival time measurements.

The Roux *et al.* (2010) method uses time-domain cross-correlation of the Rayleigh wave recorded on vertical component velocity seismograms and includes the following steps. First, we detrend and remove the mean from each event waveform and apply a two-pass, second order, Butterworth bandpass filter from 5 to 15 Hz. Next, we normalize each waveform by its peak-to-peak amplitude, assuming the largest waveform amplitude is the Rayleigh wave from a surface icequake. We select a 0.5-s window that encompasses the Rayleigh wave. For each station waveform pair we compute the time delay required to align the Rayleigh waves using time-domain cross-correlation. Initially these time delays are multiples of the sampling rates. To increase the accuracy of these time delays, we fit a quadratic function to the cross-correlation function centred on its discrete maximum. Estimating the position of the quadratic function maximum provides subsample precision.

After catalogueing time delays for each station pair we perform an inversion to solve for both the icequake location and the apparent velocity of the region. We solve the N overdetermined non-linear equations (where N is the number of time delays calculated for each source/station pair) using a quasi-Newton scheme [Tarantola & Valette 1982, eq. (25)]. A regularization term ε avoids instability during the inversion.

One source of location error stems from large uncertainties in seismic wave arrival-time measurements, which are typical for weak signals, noisy records, or deep icequakes, whose seismograms lack a well-defined Rayleigh wave. We therefore only retain the most reliable locations with waveform cross-correlations of 0.95 or above. Furthermore, we require the location scheme to successfully iterate to an acceptable solution ($<$500 iterations) and that the average standard deviation of epicentral location and velocity remains reasonable (Roux *et al.* 2010). To minimize spatial and temporal data artefacts we use only data from time periods when the full network was functioning.

Location solutions vary in quality and reliability depending on whether they are within or outside the network. We quantitatively investigate to what extent location errors vary as a function of the events being inside or outside the network using synthetic arrival times from hypothetical icequakes, whose Rayleigh waves travel at 1640 m s^{-1}. We place the hypothetical icequakes at distances between 0 and 1000 m from the network centre and at eight evenly spaced azimuths between 0° and 360°. For each icequake we produce 100 perturbed arrival time measurements by adding a normally distributed error with standard deviation of 0.05 s. Subsequently, these perturbed arrival times are inverted with our location algorithm and the distances between the inverted and actual hypothetical icequake locations are computed.

Our results show the calculated location errors (standard deviation between inverted and actual hypothetical locations) as a function of distance from the network centre (Fig. 10). These errors were averaged over all 100 perturbations and the eight azimuths. Within the network, location uncertainties are as low as a few metres, which is consistent with the error estimate of Roux *et al.* (2010). Outside the network, uncertainties in the radial direction continue to grow with distance from the network centre and quickly exceed 100 m. In contrast, and most important for this work, in the azimuthal direction the error remains constant near 2°. This azimuthal error estimation is on the conservative side, because we did not apply a quality threshold of the inversion output and because a 0.05 s arrival time error is considered high for clean surface icequake signals (Fig. 4).

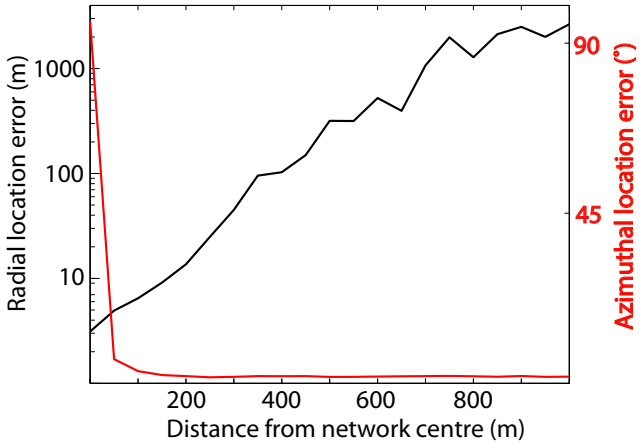

Figure 10. Error of automated icequake locations in the radial (black) and azimuthal (red) directions with respect to network centre (Fig. 2b). Note that for icequakes outside the network (>200–300 m from network centre), the azimuthal error remains constant at around 2°.

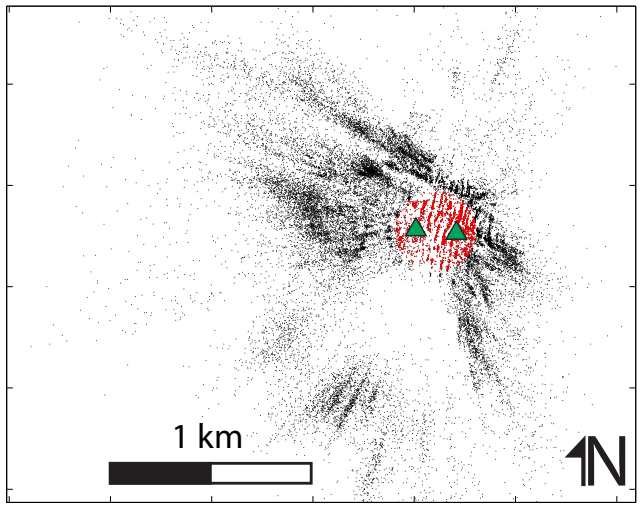

Figure 11. Epicentres of the majority of the 31 436 located surface icequakes (some epicentres locate beyond the map boundaries). Location uncertainties are as low as a few metres but quickly grow with distance from the seismometer network centre (Figs 2 and 10). Green triangles mark locations of seismometers used for subsequent cross-correlation processing. Red events are within 200 m of the two station's midpoint and therefore not used in the subsequent processing. Note that alignment of these events corresponds to the local crevasse pattern (Fig. 2).

AZIMUTHAL AVERAGE OF ICEQUAKE CROSS-CORRELATIONS

The icequake location procedure provides 31 436 acceptable surface icequake locations (Fig. 11) and determines a mean Rayleigh wave velocity of 1670 m s^{-1} with a standard deviation of 220 m s^{-1}. Within the seismic network, the epicentres form northeast to southwest trending structures, which is a manifestation of the local crevasse pattern visible in Fig. 2. This pattern is not present outside of the network due to the large location uncertainty in the radial direction.

Next we choose two stations (shown in Fig. 11 and circled in Fig. 2) and cross-correlate their *z*-component seismograms. We restrict ourselves to events that lie beyond a 200 m circular radius centred at the midpoint between the station pair (black events in Fig. 11). This leaves us with 27 116 cross-correlations (Fig. 12a),

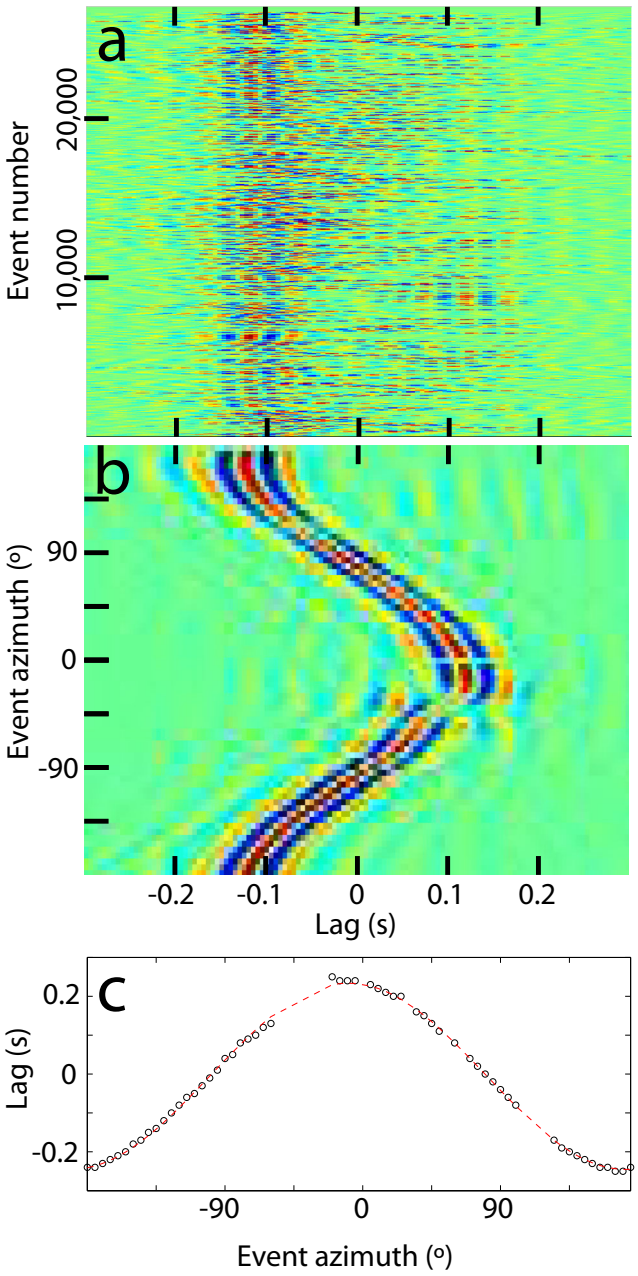

Figure 12. (a) Cross-correlation of vertical component seismograms recorded at two different seismometers for icequakes that locate more than 200 m from these stations (Fig. 11, epicentres in black). The amplitudes of the cross-correlations are colour coded, with warmer (red) and colder (blue) colours representing positive and negative amplitudes, respectively. (b) Azimuthally bin-averaged cross-correlations. (c) Sinusoidal fit to the zero lags in (b) with open black circles and dashed line representing zero lag measurements and fit, respectively. Only bin-averaged cross-correlations with maximum amplitudes above 0.6 were used.

corresponding to signals with nearly planar wave fronts at both stations.

The cross-correlation's zero lag provides an estimate of the difference in seismic wave arrival time at the two stations. Specifically, the plane wave approximation implies a sinusoidal dependence of zero lag on event azimuth. Resulting from the uneven azimuthal distribution of event epicentres (Fig. 11), there exists a bias towards negative lags (Fig. 12a).

In order to accentuate the sinusoidal relationship, we assign all cross-correlations to event azimuth bins of 5°, which is more than twice the estimated location uncertainty (Fig. 10). The sinusoidal dependence of the zero lag becomes apparent when averaging all cross-correlations within an azimuthal bin (Fig. 12b). These bin-averaged cross-correlations exhibit wavelets whose maxima are centred on the arrival time differences of the planar wave fronts. This observation bears testimony of the dominance of the direct surface wave arrival over any scattered coda. In a more heterogeneous medium that produced scattering, pre-processing would be required to remove the scattered coda from the seismograms before performing the signal cross-correlations. Without this step, the maxima of the cross-correlation would be dependent on station separation rather than plane wave incident angles (Gouédard *et al.* 2008).

We fit a sine curve to the azimuthally averaged zero lags to measure arrival time differences and thus the glacier's seismic velocity between the two stations (Fig. 12c). At the cost of a diminishing data set, we increase fit quality by discarding bin-averaged cross-correlations with maxima below 0.6.

To measure seismic velocities at different frequencies, we apply our method to octave-wide frequency ranges by bandpass filtering the icequake signals prior to correlation. We also apply a bandpass filter (5–15 Hz) during the event-location step. In order to reduce dependence on the Rayleigh wave velocity determined in the location procedure, we employ frequency ranges above 15 Hz for the sinusoidal fit approach.

We estimate velocity measurement uncertainties by first randomly drawing 1/50 of the 27 116 events used in the azimuthal bin averaging and subsequent sinusoidal fit. As our total measurement period spans nearly 57 d, these bootstrap samples, on average, include approximately the daily number of events. We thus generate 1000 bootstrap samples for which we determine the mean and standard deviation of the phase velocity measurements. For quality control, we require that the average maximum cross-correlations exceed 0.4 and that the azimuthal bins include at least 10 individual cross-correlation measurements. We require at least 10 azimuth bins satisfy these conditions. Finally, we require a sinusoidal fit variance reduction above 80 per cent and between 0.9 and 1.1 sinusoidal cycles over the full azimuthal range. These thresholds eliminate drastic outliers but never discard more than 6 per cent of the 1000 bootstrap samples.

The results (Fig. 13) show a mean Rayleigh wave velocity of around 1640 m s^{-1} with uncertainties of 50 m s^{-1} (3.1 per cent). For a glacier Poisson's ratio of 0.36 as used by Walter *et al.* (2009), this value corresponds to an *S*-velocity of 1750 m s^{-1} (using eq. 6 on page 88 in Stein & Wysession 2003). Considering uncertainties, this value is in agreement with the 1760 m s^{-1} (Walter *et al.* 2009) and 1790 m s^{-1} (Walter *et al.* 2010a,b) values used in previous waveform modelling studies of Gornergletscher icequakes.

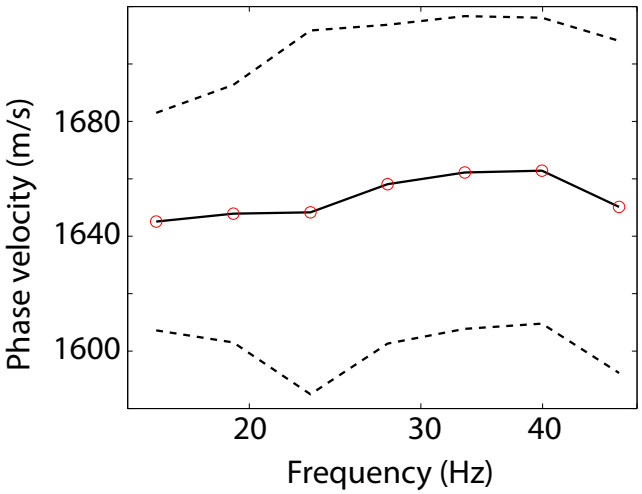

Figure 13. Rayleigh wave phase velocities for frequencies above 15 Hz measured with the icequake cross-correlation approach (red dots represent measurement points). Black solid lines and black dashed lines indicate mean and standard deviation derived from bootstrap sampling.

GREEN'S FUNCTION RETRIEVAL ON GORNERGLETSCHER

We next explore the utility of cross-correlating icequake signals. It has been shown theoretically (e.g. Wapenaar 2004; Roux *et al.* 2005; Wapenaar *et al.* 2010) and experimentally (e.g. Campillo & Paul 2003; Sabra *et al.* 2005; Denolle *et al.* 2014) that the seismic impulse response between two points in space $\mathbf{r}_1$ and $\mathbf{r}_2$ can be retrieved via cross-correlation C of noise records from both points. Confining ourselves to vertical seismograms, we can thus write:

$$\frac{\mathbf{dC}}{\mathbf{dt}} \approx -\mathbf{G}\,(\mathbf{r}_1, \mathbf{r}_2, \mathbf{t}) + G\,(\mathbf{r}_1, \mathbf{r}_2, -\mathbf{t})\,, \tag{5}$$

where t refers to time. The first term on the right hand side of the approximation describes the seismic ground motion at point $\mathbf{r}_1$ due to a force impulse at $\mathbf{r}_2$. The second term represents the time reverse of this 'Green's function', that is a wave recorded at point $\mathbf{r}_2$ due to a force impulse at $\mathbf{r}_1$.

The approximation in eq. (5) provides accurate results if attenuation is negligible and we sum over cross-correlated signals of seismic sources that evenly surround the two seismometers (Gouédard *et al.* 2008). These conditions are met in our analysis, because we restrict the cross-correlation to icequakes beyond the two stations and the azimuthal contribution of individual events is smoothed via bin averaging. Moreover, since in our case, Rayleigh waves are of primary interest, only near-surface sources have to be considered (Wapenaar *et al.* 2004).

Exploiting the relationship in eq. (5), we average the cross-correlation matrix (Fig. 12b) over all azimuth bins. This produces a wavelet at either side of $\tau = 0$ (Fig. 14a). We interpret these wavelets as the direct arrivals of the causal and acausal Green's functions between the two seismometers (Gouédard *et al.* 2008). This hypothesis can be tested with the approximation in eq. (5). Fig. 14(b) shows the time derivative of the average cross-correlation $\mathrm{d}C(\tau)/\mathrm{d}t$ together with its time and amplitude inverse $-\mathrm{d}C(-\tau)/\mathrm{d}t$. In accordance with eq. (5), the parts of these two time series corresponding to the direct arrivals show good agreement in phase and amplitude. It should be stressed that beyond the direct arrivals (i.e. $|\tau| > 0.2$ s) there also exists close agreement between the two time series shown in Fig. 14(b). This demonstrates that even though scattering is minor in glacier ice, it nevertheless generates a small Green's function coda, which we successfully recover with azimuthally averaged cross correlations.

Previous studies have shown that the direct waves of the Green's function can also be recovered when only sources in the station pair 'endfire lobes' (a small angular range around the axis connecting the two stations used for cross-correlation) are used (Gouédard *et al.* 2008). Fig. 14(c) illustrates this principle for the station pair shown

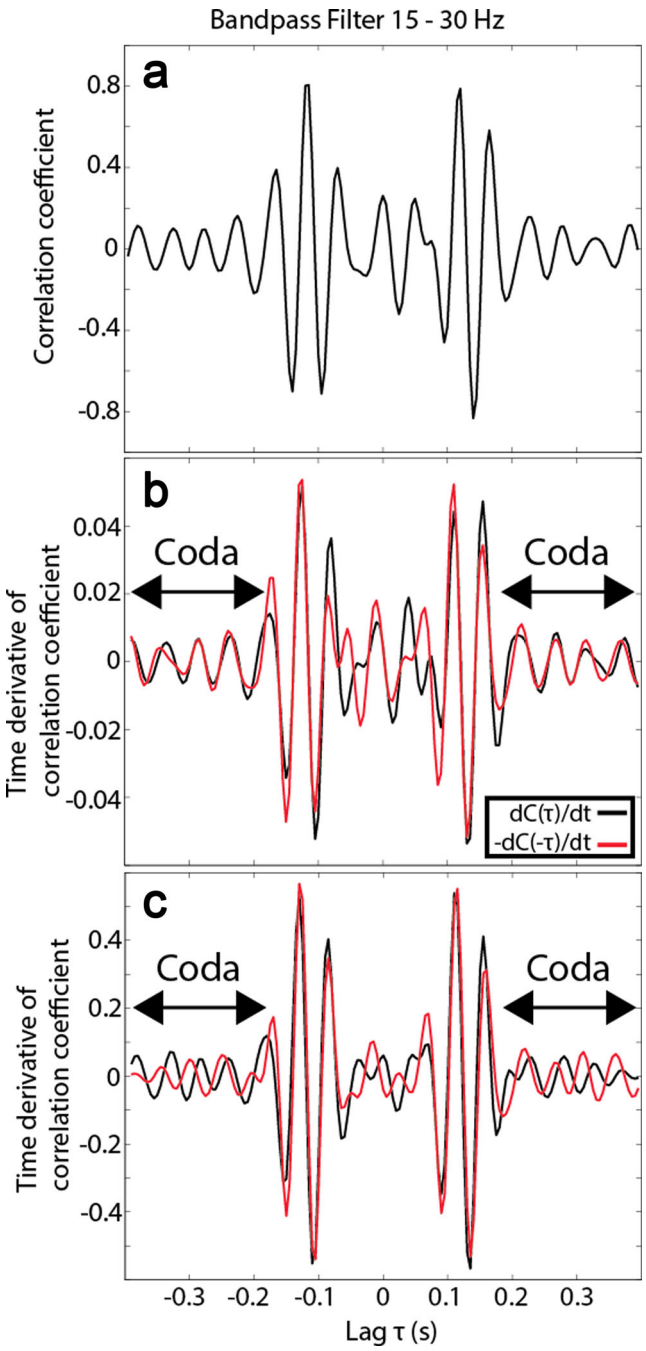

Figure 14. (a) Azimuthal average of bin-averaged cross-correlations: for each lag, the matrix shown in Fig. 12(b) was averaged over all azimuths. (b) The match between the temporal derivative of this cross-correlation and its negative time-reverse confirms that the two dominant wavelets are the causal and acausal Green's functions between the two recording seismometers (Fig. 11). (c) Recovery of direct Green's function waves is also possible when confining the azimuthal averaging to the endfire lobes. However, in this case, the Green's function coda waves are not recovered as indicated by the mismatch at lags beyond ±0.2 s.

in Fig. 11. The axis connecting the two stations has an azimuth of −6°. Averaging cross-correlations within the nearest azimuth bins (−5° and 175°) recovers a close match between the causal and acausal part of the Green's function's direct arrival. The agreement is in fact better than for the average over all bins (Fig. 14b). The reason for this is that when averaging over all azimuths, not all signal contributions from outside the endfire lobes fully cancel out as required for Green's function recovery.

Despite the successful recovery of direct Rayleigh waves, the endfire lobe averaging fails to reproduce the scattered Green's function coda. This is evident from the phase mismatch at lags beyond ±0.2 s in Fig. 14(c). This is because even though englacial scattering is minor, the scatterers that do exist near the two seismometers (mainly crevasses) are not sufficiently sampled by the waves traveling from the endfire lobes to the two seismometers. This can best be explained in the context of a single scatterer. In this case, waves traveling along the two axes connecting the scatterer and the two stations are required in addition to the endfire lobe waves (Campillo & Roux 2014). On the other hand, when using distant sources at all azimuth (Fig. 14b), the seismic waves sample more thoroughly the possible paths taken by the seismic waves between the two stations, including those of the scattered field.

MONITORING PERSPECTIVES

The presence of englacial fractures and liquid water has an influence on seismic phase velocities. The approach we present in this work to obtain phase velocity measurements using only naturally occurring seismicity can be a stepping stone for future studies that aim to monitor a glacier's subsurface structure.

In the context of engineering and ice flow dynamics there exist two particularly important processes that can be responsible for changing englacial seismic velocities. (1) Widespread fracture growth within the ice and, (2), water filling or drainage of existing fractures. Fracture growth corresponds to increases in englacial damage, which is known to accelerate prior to failure or collapse of unstable ice masses (Pralong & Funk 2005). On the other hand, changes in the water content of macroscopic englacial features (e.g. ice-walled channels, crevasses, small fissures) relate to the pressure within the subglacial drainage system. As the subglacial drainage system transitions between a low-pressure efficient and pressurized inefficient configuration, the englacial piezometric water table changes and with it the water content of connected englacial void spaces at different depths change as well (Cuffey & Paterson 2010). Importantly, the configuration of a glacier's drainage system controls basal sliding (e.g. Schoof 2010) and thus plays a key role in glacier and ice sheet dynamics. Seismic detection of water content changes in macroscopic englacial voids spaces could therefore provide important insights into the state of the subglacial drainage system.

Estimating the expected magnitude of change of seismic velocities, it is found that surface crevasses can locally decrease the *P*-wave velocity by as much as 25 per cent (Gischig 2007). The effect for *S*-waves is likely substantially larger, as elastic shear motion cannot be sustained by air or water within crevasses. For typical bulk fracture volumes of 0.3–1.3 per cent within mountain glaciers (Pohjola 1994; Harper & Humphrey 1995; Harper *et al.* 2010), we find a seismic velocity change of 1 per cent or higher reasonable when new fracture networks form or their water content changes.

USING ICEQUAKE RECORDS FOR ICE STRUCTURE MONITORING

Rayleigh waves are well suited for monitoring englacial velocity changes, because they are primarily sensitive to the *S*-wave velocity structure at a depth of approximately 1/3 of the wavelength (Li *et al.* 2013). Assuming typical *S*-velocities of around 1800 m s^{-1} in

Alpine glacier ice (Neave & Savage 1970; Deichmann *et al.* 2000; Roux *et al.* 2008), seismic velocity measurements would have to be made above 6 Hz in order to sample a glacier's top 100 m. This suggests that for monitoring purposes, icequake records are superior to moulin tremor records, because icequakes have a broadband frequency spectrum with significant energy above 30 Hz. Fig. 5(c) demonstrates this difference in frequency signature, where icequake signals appear as vertical bars covering a larger bandwidth than do the tremor signals.

Both direct waves and coda waves of Green's functions recovered with icequake cross-correlation (Fig. 14) can be used for ice structure monitoring (e.g. damage state, macroscopic water content) by means of phase velocity measurements. The advantage of using direct waves is that only azimuthal bins in the endfire lobes have to be filled reducing the number of needed icequake records. For instance, in case of Fig. 14(c), the two endfire bins contained 213 and 702 events, amounting to only 3 per cent of the data in all azimuth bins. This approach is particularly efficient when placing the seismometer pair along the direction to a known source, such as tidewater calving fronts or an active crevasse field. In these cases, the source azimuth is known, which greatly simplifies seismic processing, eliminating the need for a dense seismic network for icequake locations.

Another method to facilitate velocity measurements of direct seismic waves is to apply the sinusoidal fit to more than one station pair. We implement this method using all 60 station pairs, which are separated by 100–300 m (Fig. 15). The broad range of station separations requires us to scale the cross-correlation lag by interstation distances. We furthermore calculate the cross-correlation envelope prior to bin averaging in order to enhance constructive signal superposition. Including more than one station pair significantly increases the population within azimuthal bins (Fig. 15). For example, using only 15 icequakes produces a clear sinusoidal shape when including the 60 station pairs. Fig. 15(c) confirms that the recovered sinusoidal shape matches well with a sine function whose amplitude equals the reciprocal of the velocity determined using one station pair and all available surface icequake signals (Fig. 13).

In contrast, more than half of the azimuthal bins remain empty when using 100 icequakes with a single station pair separated by about 200 m. Therefore, using 60 station pairs allows for one phase velocity measurement every couple of minutes. On the other hand, there exist two crucial disadvantages when using more than one station pair. First, using the cross-correlation envelope decreases zero lag resolution (compare Figs 12b and 15c). Secondly, the calculated seismic velocities are spatial averages and the technique could thus not reveal lateral variations in seismic velocities. In contrast, such seismic velocity maps could be obtained when applying the single station pair cross-correlation to several station pairs throughout the network.

The disadvantage of using direct waves is that their arrival time measurements are highly sensitive to source–station distances. Changes or uncertainties in seismometer locations can thus introduce spurious changes in arrival time measurements and in turn englacial velocity estimates. For example, near our study site, englacial strain rates exceed 10^{-3} d^{-1} (Roux *et al.* 2010). Over the course of a monitoring period (a few months), interstation distances may thus change by a few per cent, masking any expected changes in seismic velocities. Consequently, as we did not continually monitor changes in station positions throughout the deployment, it is difficult to unravel to what extent the spread in phase velocity measurements determined with the bootstrap populations is caused by changes in the station positions or if the spread indeed does indicate changes in the phase velocities (Fig. 13). To do so

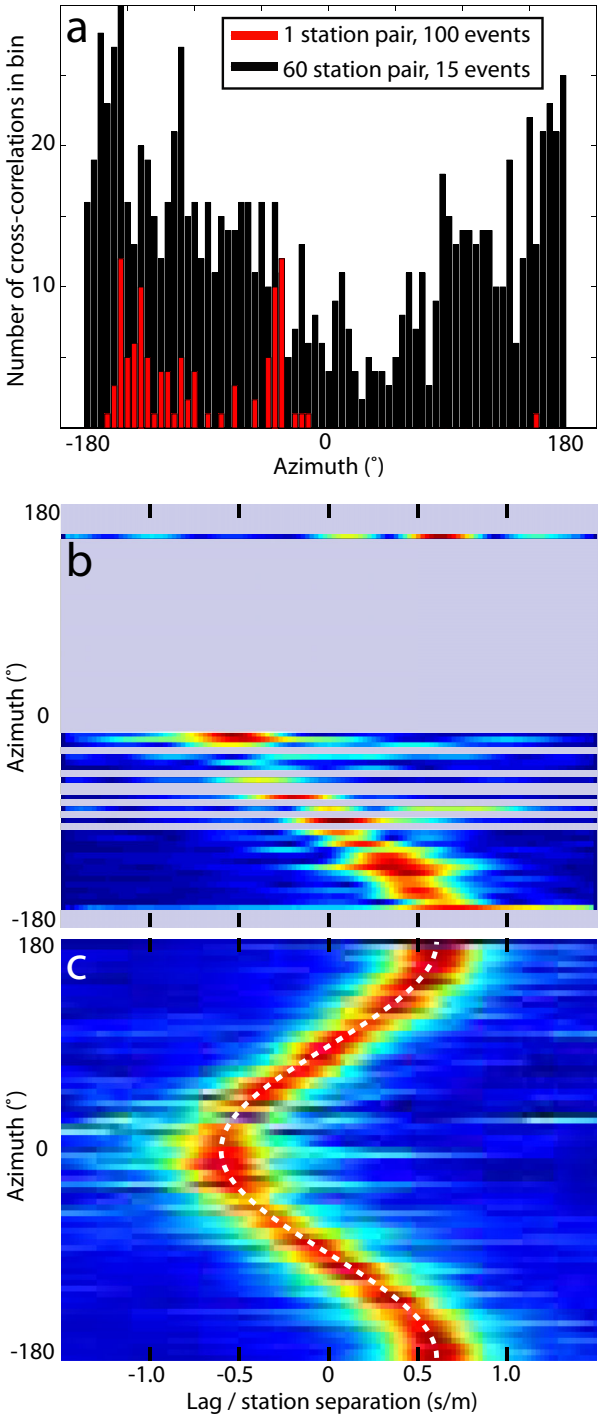

Figure 15. Bin averaging of cross-correlation envelopes using one and several station pairs and icequake records on 2006 June 6. (a) Histograms showing the populations of azimuths between station pair midpoints and icequake epicentres (in 5°-wide bins). The single station pair (red bar data) is separated by 200 m. For 100 icequakes and one station pair there is far less azimuthal coverage than for the 15 icequakes and 60 station pairs, each separated by between 100 and 300 m (black bars). (b) Bin-averaged cross-correlation for single station pair and 100 icequakes. Grey colour indicates unpopulated azimuth bins. (c) Bin-averaged cross-correlation for the 60 station pairs and 15 icequakes. White dashed line is a sine function whose amplitude is equal to the reciprocal of 1640 m s^{-1} (approximately the velocity determined in Fig. 13). Note that compared to the single-pair result (b), using several station pairs (c) allows for a faster recovery of the sinusoidal dependence of zero lag versus azimuth.

will require future networks to include differential GPS antennas collocated with the seismometers. This would allow measuring horizontal seismometer coordinates with relative uncertainties as low as 5 mm (Sugiyama *et al.* 2010), providing the necessary accuracy to compute continuous changes in inter-station distances during the network deployment.

In contrast to direct seismic waves, seismic coda waves are generated by the diffuse wave field, which is less sensitive to interstation distances. Since these coda waves travel a significantly longer distance than the direct waves, they are more sensitive to medium changes. Coda wave interferometry (Hadziioannou *et al.* 2009) has allowed for detection of seismic velocity changes less than 0.1 per cent. This technique has successfully been applied to monitoring of clay-rich landslides (Mainsant *et al.* 2012), volcanoes (Sens-Schönfelder & Wegler 2006; Benguier *et al.* 2008a) and earthquake fault zones (Brenguier *et al.* 2008a,b). The clear disadvantage of using coda waves is that icequakes at all azimuths are required, in contrast to direct wave reconstruction with endfire lobe events.

The Rayleigh wave cross-correlation location procedure of Roux *et al.* (2010) determines an icequake location and it also determines a Rayleigh wave speed as a free parameter in the non-linear inversion scheme. Our subsequent azimuthal averaging of icequake cross-correlations depends on the inverted locations and thus also on the previously determined Rayleigh wave speed. We argue that we can still use the azimuthal averaging of icequake cross-correlations to independently monitor changes of englacial velocities, because we perform this operation at 15–30 Hz, whereas the location procedure uses icequake records filtered between 5 and 15 Hz. In other words, the two procedures are most sensitive to the glacier's velocity structure at different depths. A more rigorous approach would be to measure the glacier's seismic velocity in an independent way, applying MFP to water tremor as shown above for the GrIS data. In this case, we could eliminate the Rayleigh phase velocity as a free parameter in the location routine. This would require continuous records as well as icequake seismograms of the same glacier region.

WATER TREMOR SOURCE MONITORING

Compared to broadband icequakes, coherent moulin tremor signals from the Greenland data set are confined to lower frequencies (Fig. 5). The tremor waveforms are therefore sensitive to structure at greater depths and less suited for imaging or monitoring of the shallow ice structure. Nevertheless, tremor signals contain important source property information, which can be studied with MFP.

A single station spectrogram can elucidate tremor frequency characteristics during periods of elevated moulin water level (Fig. 5). However, these individual spectrograms contain less information during low-water level conditions due to the weaker tremor signal. In contrast, focusing the matched-field beam at the tremor location, we can amplify weaker signals, which are otherwise obscured by incoherent noise sources near individual seismometers (Fig. 16). For 2011 July 29 we perform a field match using 20-min-long time windows with 3:20-min-long overlaps. As expected from the single-station spectrograms (Fig. 5), the coherence spectrograms in Fig. 16(a) are dependent on moulin water level. Consequently, in the dominant tremor frequency range (2–8 Hz), the coherence is maximal during high moulin water levels. During the rising and falling limbs of water level (above 520 m), frequencies above 9 Hz are excited, as well. This corresponds to the tremor episode start and end times when the spectrogram in Fig. 5 also reveals higher frequency content (near 17:00:00 and 01:00:00, respectively). Moreover, the high water level episodes are also associated with elevated coherence below 4 Hz. This is in agreement with the qualitative observation that spectral content tends to shift to lower frequencies during high water levels (Fig. 5).

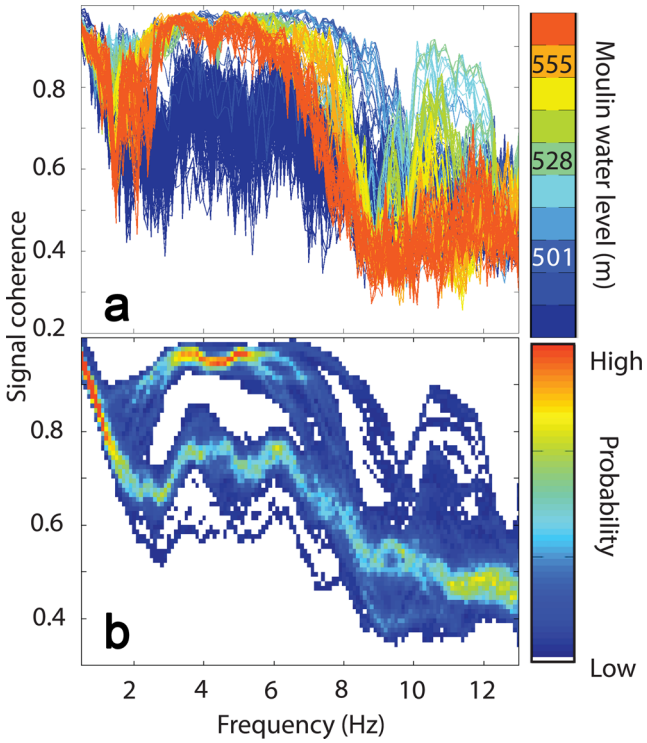

Figure 16. (a) Coherence spectra of 20-min-long moulin tremor records on 2011 July 29, colour-coded by water level within the central moulin (Fig. 1). (b) Probability density functions of smoothed coherence spectra revealing tremor frequency signature during high and low water levels within the moulin.

Even during low moulin water levels, the coherence spectra exceed 0.6 in the tremor frequency range and exhibit two spectral peaks near 4 and 6.5 Hz. These peaks are particularly apparent in the probability distribution functions of smoothed coherence spectra binned within 0.1 Hz and 0.1 units of signal coherence (panel b). These observations suggest that MFP can be used to monitor frequency characteristics of noise sources (such as englacial water flow) even for signals that are near or below the level of background noise.

CONCLUSION

This study presents two approaches to measure seismic phase velocities using signals of naturally occurring ambient sources on glaciers and ice sheets. For continuous data, matched-field processing provides Rayleigh phase dispersion curves, which can be used to estimate ice thickness. However, this method becomes less accurate with increasing bedrock topography and may thus provide only rough approximations.

Our second method that uses cross correlations of event-based icequake records constitutes a means to measure phase velocities potentially at a precision exceeding 0.1 per cent. This opens the possibility to monitor fracture growth and macroscopic water content

within glaciers without the need for active seismic sources. This approach is most efficient if nearly continuous high-precision GPS surveying of seismometer locations and both continuous and triggered icequake records are available. In this way, seismic networks can be used to monitor a glacier's subsurface structure at sub daily time scales over months or longer. This would constitute a clear advantage over active source techniques that require considerable manpower for data acquisition.

ACKNOWLEDGEMENTS

We thank the Swiss National Science Foundation and the Swiss Federal Institute of Technology (ETH Zurich) for funding seismic data collection in Greenland (grants 200021_127197 SNE-ETH and 201 ETH-27 10-3) and on Gornergletscher (Grants No. 200021-103882/1, 200020-111892/1). FW was funded by the European Union Seventh Framework Programme (FP7-PEOPLE-2011-IEF) under grant agreement n° 29919 and DK was funded by the National Science Foundation under grant EAR-1239277. The authors are grateful to Lauren Andrews, Ginny Catania, Martin Lüthi, Bob Hawley and Claudia Ryser for help in the field and for providing material to generate Figs 1, 3 and 16. Matlab® and Python together with the Waveform Suite of C. Reyes and the Obspy package (Beyreuther *et al.* 2010) were used to analyse seismic data, perform matched-field processing, cross-correlate icequake records and visualize results. Rayleigh wave dispersion was inverted using the Geopsy package (www.Geopsy.org). Satellite imagery captured by the WorldView-2 satellite and shown in Fig. 1 was provided by the Polar Geospatial Center. The inset topography map of Switzerland in Fig. 2 was created with the QPS Fledermaus software (e.g. Jacobs *et al.* 2008). The manuscript substantially benefitted from the constructive comments of the editor Gabi Laske, Sridhar Anandakrishnan and an anonymous reviewer.

REFERENCES

Aki, K. & Richards, P.G., 2002. *Quantitative Seismology,* 2nd edn, University Science Books.

Allstadt, K. & Malone, S.D., 2014. Swarms of repeating stick-slip icequakes triggered by snow loading at Mount Rainier volcano, *J. geophys. Res.: Earth Surface,* **119**(5), 1180–1203.

Amundson, J.M., Truffer, M., Lüthi, M.P., Fahnestock, M., West, M. & Motyka, R.J., 2008. Glacier, fjord, and seismic response to recent large calving events, Jakobshavn Isbræ, Greenland, *Geophys. Res. Lett.,* **35**(22), doi:10.1029/2008GL035281.

Anandakrishnan, S. & Bentley, C.R., 1993. Micro-earthquakes beneath Ice Streams Band C, West Antarctica: observations and implications, *J. Glaciol.,* **31**(133), 455–462.

Anandakrishnan, S. & Winberry, J.P., 2004. Antarctic subglacial sedimentary layer thickness from receiver function analysis, *Global planet. Change,* **42**(1), 167–176.

Andrews, L.C. *et al.*, 2014. Direct observations of evolving subglacial drainage beneath the Greenland Ice Sheet, *Nature,* **514**(7520), 80–83.

Baggeroer, A.B., Kuperman, W.A. & Mikhalevsky, P.N., 1993. An overview of matched field methods in ocean acoustics, *IEEE J. Oceanic Eng.,* **18**(4), 401–424.

Bartholomaus, T.C., Larsen, C.F., O'Neel, S. & West, M.E., 2012. Calving seismicity from iceberg–sea surface interactions, *J. geophys. Res.: Earth Surface (2003–2012),* **117**(F4), doi:10.1029/2012JF002513.

Bassis, J.N. *et al.*, 2007. Seismicity and deformation associated with ice-shelf rift propagation, *J. Glaciol.,* **53**(183), 523–536.

Bensen, G.D., Ritzwoller, M.H., Barmin, M.P., Levshin, A.L., Lin, F., Moschetti, M.P., Shapiro, N.M. & Yang, Y., 2007. Processing seismic ambient noise data to obtain reliable broad-band surface wave dispersion measurements, *Geophys. J. Int.,* **169**(3), 1239–1260.

Beyreuther, M., Barsch, R., Krischer, L., Megies, T., Behr, Y. & Wassermann, J., 2010. ObsPy: a Python toolbox for seismology, *Seismol. Res. Lett.,* **81**(3), 530–533.

Brenguier, F., Shapiro, N.M., Campillo, M., Ferrazzini, V., Duputel, Z., Coutant, O. & Nercessian, A., 2008a. Towards forecasting volcanic eruptions using seismic noise, *Nat. Geosci.,* **1**(2), 126–130.

Brenguier, F., Campillo, M., Hadziioannou, C., Shapiro, N.M., Nadeau, R.M. & Larose, E., 2008b. Postseismic relaxation along the San Andreas fault at Parkfield from continuous seismological observations, *Science,* **321**(5895), 1478–1481.

Campillo, M. & Paul, A., 2003. Long-range correlations in the diffuse seismic coda, *Science,* **299**(5606), 547–549.

Campillo, M. & Roux, P., 2014. Seismic imaging and monitoring with ambient noise correlations, in *Treatise on Geophysics*, 2nd edn., Vol. 1, pp. 256–271, eds Romanowicz, B. & Dziewonski, A., Elsevier, Amsterdam.

Carmichael, J.D., Pettit, E.C., Hoffman, M., Fountain, A. & Hallet, B., 2012. Seismic multiplet response triggered by melt at Blood Falls, Taylor Glacier, Antarctica, *J. geophys. Res.: Earth Surface (2003–2012),* **117**(F3), doi:10.1029/2011JF002221.

Chaput, J. *et al.*, 2014. The crustal thickness of West Antarctica, *J. geophys. Res.: Solid Earth,* **119**(1), 378–395.

Chen, X., Shearer, P.M., Walter, F. & Fricker, H.A., 2011. Seventeen Antarctic seismic events detected by global surface waves and a possible link to calving events from satellite images, *J. geophys. Res.: Solid Earth (1978–2012),* **116**(B6), doi:10.1029/2011JB008262.

Corciulo, M., Roux, P., Campillo, M., Dubucq, D. & Kuperman, W.A., 2012. Multiscale matched-field processing for noise-source localization in exploration geophysics, *Geophysics,* **77**(5), KS33–KS41.

Cros, E., Roux, P., Vandemeulebrouck, J. & Kedar, S., 2011. Locating hydrothermal acoustic sources at Old Faithful geyser using matched field processing, *Geophys. J. Int.,* **187**(1), 385–393.

Cuffey, K.M. & Paterson, W.S.B., 2010. *The Physics of Glaciers,* Academic Press.

Dalban Canassy, P., Walter, F., Husen, S., Maurer, H., Faillettaz, J. & Farinotti, D., 2013. Investigating the dynamics of an Alpine glacier using probabilistic icequake locations: Triftgletscher, Switzerland, *J. geophys. Res.: Earth Surface,* **118**(4), 2003–2018.

Danesi, S., Bannister, S. & Morelli, A., 2007. Repeating earthquakes from rupture of an asperity under an Antarctic outlet glacier, *Earth planet. Sci. Lett.,* **253**(1), 151–158.

Deichmann, N., Ansorge, J., Scherbaum, F., Aschwanden, A., Bernardi, F. & Gudmundsson, G.H., 2000. Evidence for deep icequakes in an Alpine glacier, *Ann. Glaciol.,* **31**(1), 85–90.

Denolle, M.A., Dunham, E.M., Prieto, G.A. & Beroza, G.C., 2014. Strong ground motion prediction using virtual earthquakes, *Science,* **343**(6169), 399–403.

Ekström, G., Nettles, M. & Abers, G.A., 2003. Glacial earthquakes, *Science,* **302**(5645), 622–624.

Gischig, V., 2007. Seismic Investigations on Gornergletscher, *Diploma thesis,* Abteilung für Glaziologie, VAW (unpublished), ETH–Zürich.

Gouédard, P., Roux, P., Campillo, M. & Verdel, A., 2008. Convergence of the two-point correlation function toward the Green's function in the context of a seismic-prospecting data set, *Geophysics,* **73**(6), V47–V53.

Hadziioannou, C., Larose, E., Coutant, O., Roux, P. & Campillo, M., 2009. Stability of monitoring weak changes in multiply scattering media with ambient noise correlation: laboratory experiments, *J. acoust. Soc. Am.,* **125**(6), 3688–3695.

Harland, S.R. *et al.*, 2013. Deformation in Rutford Ice Stream, West Antarctica: measuring shear-wave anisotropy from icequakes, *Ann. Glaciol.,* **54**(64), 105–114.

Harper, J.T. & Humphrey, N.F., 1995. Borehole video analysis of a temperate glacier's englacial and subglacial structure: implications for glacier flow models, *Geology,* **23,** 901–904.

Harper, J.T., Bradford, J.H., Humphrey, N.F. & Meierbachtol, T.W., 2010. Vertical extension of the subglacial drainage system into basal crevasses, *Nature,* **467**(7315), 579–582.

Heeszel, D.S., Fricker, H.A., Bassis, J.N., O'Neel, S. & Walter, F., 2014. Seismicity within a propagating ice shelf rift: the relationship between

icequake locations and ice shelf structure, *J. geophys. Res.: Earth Surface,* **119**(4), 731–744.

Hoffman, M.J., Catania, G.A., Neumann, T.A., Andrews, L.C. & Rumrill, J.A., 2011. Links between acceleration, melting, and supraglacial lake drainage of the western Greenland Ice Sheet, *J. geophys. Res.: Earth Surface (2003–2012),* **116**(F4), doi:10.1029/2010JF001934.

Huss, M., 2005. Gornergletscher — Gletscherseeausbrüche und Massenbilanzabschätzungen (in german with english summary), *Diploma thesis,* Abteilung für Glaziologie, VAW (unpublished), ETH–Zürich, pp. 176.

Jacobs, A.M., Kilb, D. & Kent, G., 2008. 3-D interdisciplinary visualization: tools for scientific analysis and communication, *Seismol. Res. Lett.,* **79**(6), 867–876.

Kohnen, H., 1974. The temperature dependence of seismic waves in ice, *J. Glaciol.,* **13,** 144–147.

Larmat, C., Tromp, J., Liu, Q. & Montagner, J.P., 2008. Time reversal location of glacial earthquakes, *J. geophys. Res.: Solid Earth (1978–2012),* **113**(B9), doi:10.1029/2008JB005607.

Li, L., Li, A., Shen, Y., Sandvol, E.A., Shi, D., Li, H. & Li, X., 2013. Shear wave structure in the northeastern Tibetan Plateau from Rayleigh wave tomography, *J. geophys. Res.: Solid Earth,* **118,** doi:10.1002/jgrb.50292.

Lipovsky, B.P. & Dunham, E.M., 2015. Vibrational modes of hydraulic fractures: inference of fracture geometry from resonant frequencies and attenuation, *J. geophys. Res.,* **120,** 1080–1107.

Mainsant, G., Larose, E., Brönnimann, C., Jongmans, D., Michoud, C. & Jaboyedoff, M., 2012. Ambient seismic noise monitoring of a clay landslide: toward failure prediction, *J. geophys. Res.,* **117,** F01030, doi:10.1029/2011JF002159.

Maupin, V., 2007. Introduction to mode coupling methods for surface waves, *Adv. Geophys.,* **48,** 127–155.

McGrath, D., Colgan, W., Steffen, K., Lauffenburger, P. & Balog, J., 2011. Assessing the summer water budget of a moulin basin in the Sermeq Avannarleq ablation region, Greenland ice sheet, *J. Glaciol.,* **57**(205), 954–964.

Mikesell, T.D., Wijk, K., Haney, M.M., Bradford, J.H., Marshall, H.P. & Harper, J.T., 2012. Monitoring glacier surface seismicity in time and space using Rayleigh waves, *J. geophys. Res.: Earth Surface (2003–2012),* **117**(F2), doi:10.1029/2011JF002259.

Moore, P.L., Winberry, J.P., Iverson, N.R., Christianson, K.A., Anandakrishnan, S., Jackson, M., Mathison, M. & Cohen, D., 2013. Glacier slip and seismicity induced by surface melt, *Geology,* **41**(12), 1247–1250.

Neave, K.G. & Savage, J.C., 1970. Icequakes on the Athabasca glacier, *J. geophys. Res.,* **75**(8), 1351–1362.

Nettles, M. & Ekström, G., 2010. Glacial earthquakes in Greenland and Antarctica, *Ann. Rev. Earth planet. Sci.,* **38**(1), 467–491.

O'Neel, S., Marshall, H.P., McNamara, D.E. & Pfeffer, W.T., 2007. Seismic detection and analysis of icequakes at Columbia Glacier, Alaska, *J. geophys. Res.: Earth Surface (2003–2012),* **112**(F3), doi:10.1029/2006JF000595.

Pohjola, V.A., 1994. TV-video observations of englacial voids in Storglaciaren, Sweden, *J. Glaciol.,* **40,** 231–240.

Pomeroy, J., Brisbourne, A., Evans, J. & Graham, D., 2013. The search for seismic signatures of movement at the glacier bed in a polythermal valley glacier, *Ann. Glaciol.,* **54**(64), 149–156.

Pralong, A. & Funk, M., 2005. Dynamic damage model of crevasse opening and application to glacier calving, *J. geophys. Res.: Solid Earth (1978–2012),* **110**(B1), doi:10.1029/2004JB003104.

Pratt, M.J., Winberry, J.P., Wiens, D.A., Anandakrishnan, S. & Alley, R.B., 2014. Seismic and geodetic evidence for grounding-line control of Whillans Ice Stream stick-slip events, *J. geophys. Res.: Earth Surf.,* **119**(2), 333–348.

Richardson, J.P., Waite, G.P., FitzGerald, K.A. & Pennington, W.D., 2010. Characteristics of seismic and acoustic signals produced by calving, Bering Glacier, Alaska, *Geophys. Res. Lett.,* **37**(3), doi:10.1029/2009GL041113.

Röösli, C., Walter, F., Husen, S., Andrews, L.C., Lüthi, M.P., Catania, G.A. & Kissling, E., 2014. Sustained seismic tremors and icequakes detected in the ablation zone of the Greenland ice sheet, *J. Glaciol.,* **60**(221), 563.

Roux, P., Sabra, K.G., Kuperman, W.A. & Roux, A., 2005. Ambient noise cross correlation in free space: theoretical approach, *J. acoust. Soc. Am.,* **117**(1), 79–84.

Roux, P.F., Marsan, D., Métaxian, J.P., O'Brien, G. & Moreau, L., 2008. Microseismic activity within a serac zone in an alpine glacier (Glacier d'Argentière, Mont Blanc, France), *J. Glaciol.,* **54**(184), 157–168.

Roux, P.F., Walter, F., Riesen, P., Sugiyama, S. & Funk, M., 2010. Observation of surface seismic activity changes of an Alpine glacier during a glacier-dammed lake outburst, *J. geophys. Res.: Earth Surface (2003–2012),* **115**(F3), doi:10.1029/2009JF001535.

Ryser, C., Lüthi, M.P., Andrews, L.C., Hoffman, M.J., Catania, G.A., Hawley, R.L., Neumann, T.A. & Kristensen, S.S., 2014. Sustained high basal motion of the Greenland ice sheet revealed by borehole deformation, *J. Glaciol.,* **60**(222), 647, doi:10.3189/2014JoG13J196.

Sabra, K.G., Gerstoft, P., Roux, P., Kuperman, W.A. & Fehler, M.C., 2005. Extracting time-domain Green's function estimates from ambient seismic noise, *Geophys. Res. Lett.,* **32**(3), doi:10.1029/2004GL021862.

Schoof, C., 2010. Ice-sheet acceleration driven by melt supply variability, *Nature,* **468**(7325), 803–806.

Sens-Schönfelder, C. & Wegler, U., 2006. Passive image interferometry and seasonal variations of seismic velocities at Merapi Volcano, Indonesia, *Geophys. Res. Lett.,* **33**(21), doi:10.1029/2006GL027797.

Smith, A.M., 2006. Microearthquakes and subglacial conditions, *Geophys. Res. Lett.,* **33**(24), doi:10.1029/2006GL028207.

St. Lawrence, W. & Qamar, A., 1979. Hydraulic transients: a seismic source in volcanoes and glaciers, *Science,* **203**(4381), 654–656.

Stein, S. & Wysession, M., 2003. *An Introduction to Seismology, Earthquakes, and Earth Structure,* Blackwell Publishing.

Sugiyama, S., Bauder, A., Riesen, P. & Funk, M., 2010. Surface ice motion deviating toward the margins during speed-up events at Gornergletscher, Switzerland, *J. geophys. Res.,* **115,** F03010, doi:10.1029/2009JF001509.

Tarantola, A. & Valette, B., 1982. Generalized nonlinear inverse problems solved using the least squares criterion, *Rev. Geophys.,* **20**(2), 219–232.

Thelen, W.A., Allstadt, K., De Angelis, S., Malone, S.D., Moran, S.C. & Vidale, J., 2013. Shallow repeating seismic events under an alpine glacier at Mount Rainier, Washington, USA, *J. Glaciol.,* **59**(214), 345–356.

Tsai, V.C. & Ekström, G., 2007. Analysis of glacial earthquakes, *J. geophys. Res.: Earth Surface (2003–2012),* **112**(F3), doi:10.1029/2006JF000596.

Vandemeulebrouck, J. *et al.*, 2010. Application of acoustic noise and self-potential localization techniques to a buried hydrothermal vent (Waimangu Old Geyser site, New Zealand), *Geophys. J. Int.,* **180**(2), 883–890.

Vandemeulebrouck, J., Roux, P. & Cros, E., 2013. The plumbing of Old Faithful Geyser revealed by hydrothermal tremor, *Geophys. Res. Lett.,* **40**(10), 1989–1993.

Veitch, S.A. & Nettles, M., 2012. Spatial and temporal variations in Greenland glacial-earthquake activity, 1993–2010, *J. geophys. Res.: Earth Surface (2003–2012),* **117**(F4), doi:10.1029/2012JF002412.

Walter, F., 2009. Seismic activity on Gornergletscher during Gornersee outburst floods, *Doctoral dissertation,* Eidgenössische Technische Hochschule ETH Zürich, Nr. 18184, 2009.

Walter, F., Deichmann, N. & Funk, M., 2008. Basal icequakes during changing subglacial water pressures beneath Gornergletscher, Switzerland, *J. Glaciol.,* **54**(186), 511–521.

Walter, F., Clinton, J.F., Deichmann, N., Dreger, D.S., Minson, S.E. & Funk, M., 2009. Moment tensor inversions of icequakes on Gornergletscher, Switzerland, *Bull. seism. Soc. Am.,* **99**(2A), 852–870.

Walter, F., O'Neel, S., McNamara, D., Pfeffer, W.T., Bassis, J.N. & Fricker, H.A., 2010a. Iceberg calving during transition from grounded to floating ice: Columbia Glacier, Alaska, *Geophys. Res. Lett.,* **37**(15), doi:10.1029/2010GL043201.

Walter, F., Dreger, D.S., Clinton, J.F., Deichmann, N. & Funk, M., 2010b. Evidence for near-horizontal tensile faulting at the base of Gornergletscher, a Swiss Alpine Glacier, *Bull. seism. Soc. Am.,* **100**(2), 458–472.

Walter, J.I., Brodsky, E.E., Tulaczyk, S., Schwartz, S.Y. & Pettersson, R., 2011. Transient slip events from near-field seismic and geodetic data on a glacier fault, Whillans Ice Plain, West Antarctica, *J. geophys. Res.: Earth Surface (2003–2012),* **116**(F1), doi:10.1029/2010JF001754.

Walter, F., Amundson, J.M., O'Neel, S., Truffer, M., Fahnestock, M. & Fricker, H.A., 2012. Analysis of low-frequency seismic signals generated during a multiple-iceberg calving event at Jakobshavn Isbræ, Greenland, *J. geophys. Res.: Earth Surface (2003–2012),* **117**(F1), doi:10.1029/2011jf002132.

Walter, F., Chaput, J. & Lüthi, M.P., 2014. Thick sediments beneath Greenland's ablation zone and their potential role in future ice sheet dynamics, *Geology,* **42**(6), 487–490.

Wapenaar, K., 2004. Retrieving the elastodynamic Green's function of an arbitrary inhomogeneous medium by cross correlation, *Phys. Rev. Lett.,* **93**(25), 254301, doi:10.1103/PhysRevLett.93.254301.

Wapenaar, K., Slob, E., Snieder, R. & Curtis, A., 2010. Tutorial on seismic interferometry: Part 2—underlying theory and new advances, *Geophysics,* **75**(5), 75A 211–75A 227.

Wathelet, M., 2008. An improved neighborhood algorithm: parameter conditions and dynamic scaling, *Geophys. Res. Lett.,* **35**(9), doi:10.1029/2008GL033256.

West, M.E., Larsen, C.F., Truffer, M., O'Neel, S. & LeBlanc, L., 2010. Glacier microseismicity, *Geology,* **38**(4), 319–322.

Wiens, D.A., Anandakrishnan, S., Winberry, J.P. & King, M.A., 2008. Simultaneous teleseismic and geodetic observations of the stick–slip motion of an Antarctic ice stream, *Nature,* **453**(7196), 770–774.

Winberry, P.J., Anandakrishnan, S., Wiens, D.A. & Alley, R.B., 2013. Nucleation and seismic tremor associated with the glacial earthquakes of Whillans Ice Stream, Antarctica, *Geophys. Res. Lett.,* **40**(2), 312–315.

Wittlinger, G. & Farra, V., 2012. Observation of low shear wave velocity at the base of the polar ice sheets: evidence for enhanced anisotropy, *Geophys. J. Int.,* **190**(1), 391–405.

Zhan, Z., Tsai, V.C., Jackson, J.M. & Helmberger, D., 2014. Ambient noise correlation on the Amery Ice Shelf, East Antarctica, *Geophys. J. Int.,* **196**(3), 1796–1802.

Zoet, L.K., Anandakrishnan, S., Alley, R.B., Nyblade, A.A. & Wiens, D.A., 2012. Motion of an Antarctic glacier by repeated tidally modulated earthquake, *Nat. Geosci.,* **5**(9), 623–626.